

Structure–Property–Functionality of Bimetal Interfaces

I. J. BEYERLEIN,^{1,3} N. A. MARA,¹ J. WANG,¹ J. S. CARPENTER,¹
S. J. ZHENG,¹ W. Z. HAN,¹ R. F. ZHANG,¹ K. KANG,¹ T. NIZOLEK,²
and T. M. POLLOCK²

1.—Los Alamos National Laboratory, Los Alamos, NM 87545, USA. 2.—University of California at Santa Barbara, Santa Barbara, CA 93106, USA. 3.—e-mail: irene@lanl.gov

Interfaces, such as grain boundaries, phase boundaries, and surfaces, are important in materials of any microstructural size scale, whether the microstructure is coarse-grained, ultrafine-grained, or nano-grained. In nanostructured materials, however, they dominate material response and as we have seen many times over, can lead to extraordinary and unusual properties that far exceed those of their coarse-grained counterparts. In this article, we focus on bimetal interfaces. To best elucidate interface structure–property–functionality relationships, we focus our studies on simple layered composites composed of an alternating stack of two metals with bimetal interfaces spaced less than 100 nm. We fabricate these nanocomposites by either a bottom–up method (physical vapor deposition) or a top–down method (accumulative roll bonding) to produce two distinct interface types. Atomic-scale differences in interface structure are shown to result in profound effects on bulk-scale properties.

MATERIALS WITH UNUSUALLY HIGH INTERFACE CONTENT

Future energy technologies demand novel materials that tolerate extremes in temperature, strain, strain rate, and radiation to an extent that far exceeds the limits of even the most advanced materials to date. To meet these needs, promising new material candidates are nanostructured multiphase/multi-interface materials, such as oxide dispersion-strengthened steels, multilayered nanocomposites, and nanotwinned nanocrystalline copper. In the semiconductor industry, length scales of metallic interconnects and microelectromechanical devices already are well under 100 nm, and their reliability depends, in part, on mechanical robustness under thermal cycling, vibration, and in some cases, radiation damage tolerance. Such nanoscale multiphase composite metals contain an unusually high density of heterophase interfaces to an extent that the bimetal interfaces control all defect-related processes. Quite unconventionally, the constituent nanoscale phases play a secondary role. With the “right” characteristics, these bimaterial interfaces can possess significantly enhanced abilities to absorb and eliminate defects, granting the parent composite a highly effective healing mechanism and an unparalleled ability to mitigate damage accumulation induced

under severe loading conditions and/or environments. For instance, experimental tests on multilayered Cu-Nb composites with nanothick layers exhibit outstanding thermal stability,¹ ultrahigh strength,^{2,3} simultaneous ductility,^{3,4} shock resistance,⁵ and radiation resistance,⁶ undeniably outperforming their constituents by orders of magnitude.

Model Materials: Multilayer Composites

Nanostructured composites clearly possess superior properties that we wish to harness and exploit but at present, we do not completely understand. We can easily rationalize that their extraordinary behavior is due to high interfacial content and some exceptional qualities the interfaces have. However, to progress to the next level of prediction and control, we need to better understand the structure–property–functionality relationships of interfaces starting from the atomic level to the mesoscale. Achieving this is facilitated with the use of model materials, materials that we can synthesize, characterize, and model simultaneously. Model materials themselves may not be used directly in application, but they help us gain tremendous fundamental insight. For our purposes, small-scale studies are performed on multilayered, two-phase composites. These are two-dimensional planar composites consisting of an

alternating stack of two metals. The metals are immiscible and, thus, do not chemically mix at the interface. For the nanolength scales of interest, the individual layers are on the order of 100 nm or less and are a single grain thick. The grains are several times wider than the thickness and thus, the composite contains more bimetal interfacial area than grain boundary area.

Top Down Versus Bottom Up

Multilayered composite materials with high interfacial content can be made in two ways, one via a bottom–up process such as physical vapor deposition (PVD) in the form of a composite film or two via a top–down process such as accumulative roll bonding (ARB) in the form of a bulk sample. Both methods are capable of fabricating two-dimensional planar nanocomposites with controllable phase sizes down to the nanoscale (varying from 100 nm to less than 5 nm). However, the former method fabricates samples in the form of thin films (usually a few microns thick) with thermally preferred interfaces while the ARB technique makes sheet material in bulk form ($> \text{cm}^3$) with mechanically driven interfaces.

Figure 1a schematically lays out the ARB materials processing approach for fabricating bulk two-phase layered composites. The ARB process consists of repeated rolling, sectioning, stacking, bonding, and rerolling. With ARB, two-phased (Cu–Nb) ARB samples with controllable layer thicknesses h from submicron to the nanoscale (down to 9 nm) are possible, as shown in Fig. 1b, c. Notably, for all h , the Cu–Nb interfaces are flat, planar, and sharp, providing for little chemical variation in the interface plane. Submicron and nanostructured Cu–Nb nanocomposites have also been fabricated in bulk using other top–down synthesis techniques, such as wire drawing⁷ and equal-channel angular extrusion.⁸

The ARB composites share the same nanolamellar stacked architecture as the PVD nanolayers; however, as our microstructural analysis reveals, the interfaces are remarkably different. The specific Cu–Nb interface structure that is created during PVD can adopt the classical Kurdjumov–Sachs (KS) or Nishiyama–Wasserman (NW) orientation relationship joined at the $\{111\}\text{Cu} \parallel \{110\}\text{Nb}$ interface planes, as characterized by diffraction techniques and transmission electron microscopy (TEM).⁹ For ARB composites, on the other hand, it is not known whether the resulting interfacial orientations and structures are uniform, as in the PVD foil, or inhomogeneous. Only recently has it been possible to characterize interfaces at a fine scale but over a large volume of the material, such that statistically significant sets of interfaces can be characterized.¹⁰ This is accomplished for both PVD and ARB Cu–Nb composites with application of an automated heterophase interface characterization distribution (HICD) method to electron backscatter diffraction

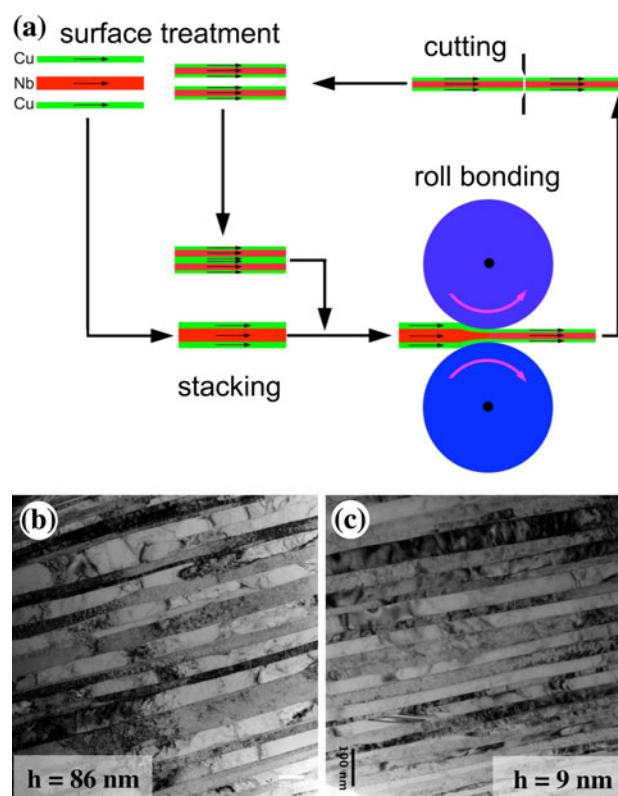


Fig. 1. (a) Schematic of the ARB process for top–down synthesis of multilayered nanocomposites. As shown, the Cu–Nb stack initially has terminating half-thick Cu layers on the top and bottom. In this way, no new Cu–Nb interfaces are created during the restacking step, new bonds are always between Cu/Cu, and Cu and Nb maintain nominally equal thickness. TEM micrographs of Cu–Nb ARB composites of different layer thicknesses h , (b) a nominal layer thickness of $h = 86$ nm, and (c) $h = 9$ nm, containing 5184 individual layers and achieved by subjecting the material to a total Von Mises strain of 12.21.

(EBSD) data.¹⁰ The HICD method marches along the interface visible in EBSD and determines the five parameters that define the interface crystallography (e.g., three for the orientation relationship and two for the interface plane). For ARB composites with submicron layer thicknesses, ~ 200 – 600 nm, the HICD method is particularly advantageous over diffraction techniques when there is more than one grain through the thickness or when the interface is rough (i.e., the interface plane varies). For instance, crystals associated with the interface can be distinguished from those within the phase. For the ARB material, a remarkable discovery revealed by the HICD method is the development of a narrow distribution of interface orientation relationships after extreme straining. A $\{112\}\text{fcc} \parallel \{112\}\text{bcc} \langle 110 \rangle \text{fcc} \parallel \langle 111 \rangle \text{bcc}$ interface appeared to prevail over the entire sample.¹⁰ With respect to the rolled sample axis, the in-plane $\langle 110 \rangle \text{fcc} \parallel \langle 111 \rangle \text{bcc}$ directions are aligned along the transverse direction (TD) and $\langle 111 \rangle \text{fcc} \parallel \langle 110 \rangle \text{bcc}$ along the rolling direction (RD). For the purposes of characterizing the microstructure at finer length scales, when the layers are a

single grain thick, we also carried out high-resolution TEM (HRTEM), TEM, neutron diffraction analyses^{11–13} as well as a relatively new characterization method, precession electron diffraction,¹⁴ which combines orientation and phase mapping in the TEM. These techniques confirmed that the $\{112\}_{\text{fcc}}\|\{112\}_{\text{bcc}}$ $\langle 110 \rangle_{\text{fcc}}\|\langle 111 \rangle_{\text{bcc}}$ interface prevails even under further straining and higher bimetal densities. This interface differs from the $\{111\}_{\text{Cu}}\|\{110\}_{\text{Nb}}$ KS interfaces in the PVD Cu-Nb nanolayered thin films. While it shares the same KS-orientation relationship it instead joins the Cu and Nb at their mutual $\{112\}$ planes. Interestingly this same interface has been found using TEM in severely wire-drawn Cu-Nb composites^{15,16} and in Ni-Cr alloys.^{17,18} Another interface $\{110\}_{\text{fcc}}\|\{112\}_{\text{bcc}}$ $\langle 110 \rangle_{\text{fcc}}\|\langle 111 \rangle_{\text{bcc}}$ was also found by the HICD method, although it occurred less frequently.

The Role of Interfaces

We now have two model multilayer composites with nearly the same architecture, but different prevailing interfaces: (1) $\{111\}_{\text{Cu}}\|\{110\}_{\text{Nb}}$ KS interfaces in the PVD Cu-Nb nanolayered thin films and (2) $\{112\}_{\text{fcc}}\|\{112\}_{\text{bcc}}$ KS interfaces in the ARB Cu-Nb nanolayered bulk material. Atomic-level to macroscale-level studies of these two materials will lead to vastly improved understanding how interface structure impacts interface properties and how these properties drive material behavior in deformation and other nonequilibrium conditions. In this article, the knowledge gained to date is compiled with the aim of relating the three levels shown in Fig. 2a. Ultimately, such understanding can lead the way towards controlling composite fabrication to achieve target interfacial properties for desired material performance.

The Structure–Energy–Kinetics Triad

When comparing two different interfaces in terms of their stability during mechanical deformation or elevated temperatures, we need to invoke some measures of quality. To this end, there are three aspects to consider: structure, energy, and kinetics (Fig. 2b). The first, interface structure, includes features ranging from atomic-scale interfacial steps to the nanoscale network of misfit dislocations. The second, energy-related properties, are interface formation energy and energy of a vacancy or extrinsic dislocation within the interface, for example. The last, kinetic-related properties, involve ways in which the interface supports plastic slip, via dislocation nucleation, dislocation transmission, or dislocation reactions. Below, we compare the $\{111\}_{\text{Cu}}\|\{110\}_{\text{Nb}}$ KS interface in PVD Cu-Nb composites with the $\{112\}_{\text{Cu}}\|\{112\}_{\text{Nb}}$ KS interface in Cu-Nb ARB composites with respect to their structure, energy, and kinetic properties.

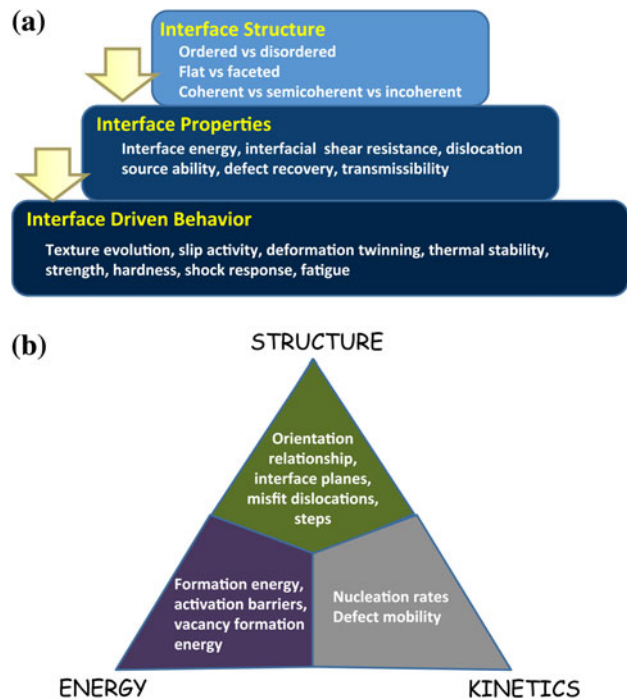


Fig. 2. (a) Structure–property–functionality relationships of bimetal interfaces: top, interface structural characteristics; middle, interface properties; bottom, interface-driven behavior. (b) Defining the quality of an interface based on its structural, energetic, and kinetic aspects.

STRUCTURE

Atomically Flat Versus Atomically Stepped Interfaces

Structure governs the energetic and kinetic aspects and thus is described first. TEM characterization and atomistic simulations have shown that the PVD interfaces that join $\{111\}_{\text{fcc}}\|\{110\}_{\text{bcc}}$ planes, and are atomically sharp, ordered (possessing a well-defined pattern of misfits), and flat (Fig. 3a, b⁹). These interfaces have either a KS or NW orientation relationship. (The NW interface deviates from the KS interface by a $\sim 5^\circ$ twist about the interface normal.) As for the two predominant interfaces found in the ARB composites, only a small number of microscopy and molecular dynamics (MD) simulation studies has examined the $\{112\}\langle 111 \rangle_{\text{fcc}}\|\{112\}\langle 110 \rangle_{\text{bcc}}$ interface^{11,12,15–20} and even fewer the $\{110\}_{\text{fcc}}\|\{112\}_{\text{bcc}}$ interface. HRTEM micrographs of these two interfaces in nanocomposites fabricated by ARB are shown in Fig. 3c, d. The three distinct features common among the ARB interfaces are that they are ordered, containing regular arrays of misfits; are stepped, containing a regular array of facets; and have the compact directions of the fcc and bcc crystals aligned $\langle 110 \rangle_{\text{fcc}}\|\langle 111 \rangle_{\text{bcc}}$ along the TD.²⁰

As a complementary way to characterize interface structure, atomic-scale models and atomistic simulations have been used to reveal the details of interface structure and characterize the defects it contains.^{17,19–22} With MD simulation, the relaxed

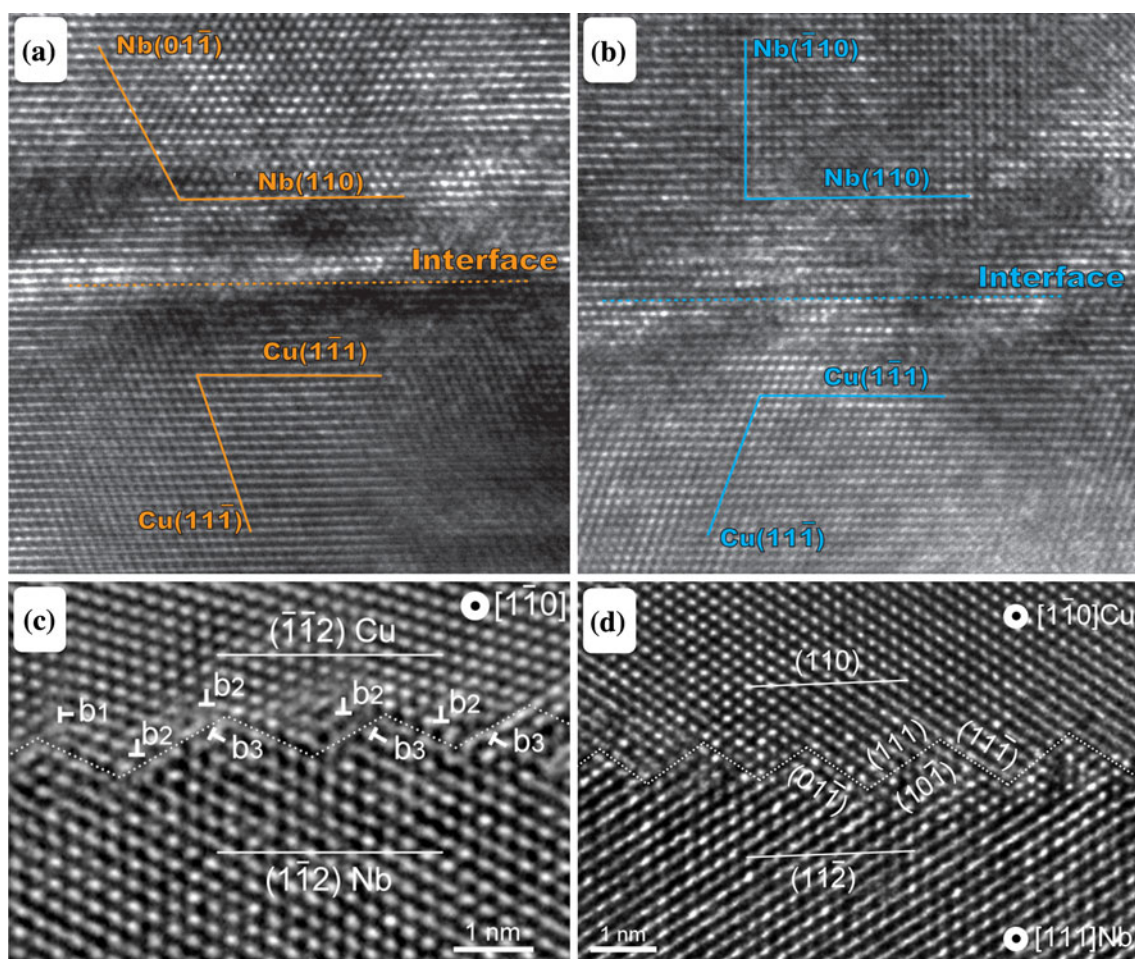


Fig. 3. HRTEM micrographs of a (a) $\{111\}$ fcc $\parallel\{110\}$ bcc KS interface in a Cu-Nb PVD nanolayered composite;⁹ (b) $\{111\}$ fcc $\parallel\{110\}$ bcc NW interface in a Cu-Nb PVD nanolayered composite; (c) $\{112\}$ fcc $\parallel\{112\}$ bcc KS interface in a Cu-Nb ARB composite ($h = 18$ nm), containing an array of edge dislocations oriented along $[\bar{1}10]$ with a Burgers vector of $\mathbf{b}_2 = 1/3[111]$, which lies in the plane of the interface; and (d) $\{110\}$ fcc $\parallel\{112\}$ bcc interface in a Cu-Nb ARB composite ($h = 30$ nm).

atomic structures of the $\{111\}$ fcc $\parallel\{110\}$ bcc KS and $\{112\}$ fcc $\parallel\{112\}$ bcc KS interfaces are found to be remarkably distinct. Figure 4 compares the relaxed equilibrium atomic structure of the (Fig. 4a, b) PVD $\{111\}$ fcc $\parallel\{110\}$ bcc KS interface with the (Fig. 4c, d) ARB $\{112\}$ fcc $\parallel\{112\}$ bcc KS interface. The simulation finds that both interfaces are ordered, containing a regular network of interfacial misfit dislocations, as shown in Fig. 4c, d. The dislocation interfacial network accommodates the mismatch between the two lattices at the planes where they are joined.

Consistent with the HRTEM analysis, MD simulation finds that these two interfaces differ in their facet features and the Burgers vectors of their misfit dislocations. The reason the facets form in one and not the other is clear. The unrelaxed $\{112\}$ planes of the Cu and Nb crystals are serrated (see Fig. 2b in Wang et al.,²² this issue) and when joined and relaxed at an interface, the stepped feature we see in Fig. 4c forms. The facet structure alternates between the (001) Cu $\parallel(101)$ Nb terrace planes and

$(11\bar{1})$ Cu $\parallel(0\bar{1}1)$ Nb terrace planes along the interface. To accommodate the in-plane and out-of-plane mismatch across the Cu and Nb $\{112\}$ planes, the $\{112\}$ fcc $\parallel\{112\}$ bcc KS contains misfit interfacial dislocation with Burgers vectors with either an in-plane or out-of-plane component. The plan view of this interface in Fig. 4d shows readily the dislocation lines making up the interface dislocation network. The $\{112\}$ fcc $\parallel\{112\}$ bcc KS consists of three distinct sets of misfit dislocations, two \mathbf{b}_1 and \mathbf{b}_2 , which are oriented parallel to the $[\bar{1}10]$ fcc $\parallel[1\bar{1}\bar{1}]$ bcc axis and the third \mathbf{b}_3 oriented parallel to the $[111]$ fcc $\parallel[110]$ bcc axis. The first array contains dislocations $\mathbf{b}_1 = \mathbf{b}_N$ each with a net out-of-plane Burgers vector of 2.95 Å, directed normal to the interface plane, and spaced 18.7 Å apart. As shown in Fig. 4c, this array of misfits has already dissociated into a residual that remains in the interface and a Shockley partial $\mathbf{b}_S = a_{Cu}[\bar{1}\bar{1}2]/6$ that clearly extends a finite amount from the interface onto the (111) plane of Cu, creating a stacking fault. The second set that lies parallel to the first has an

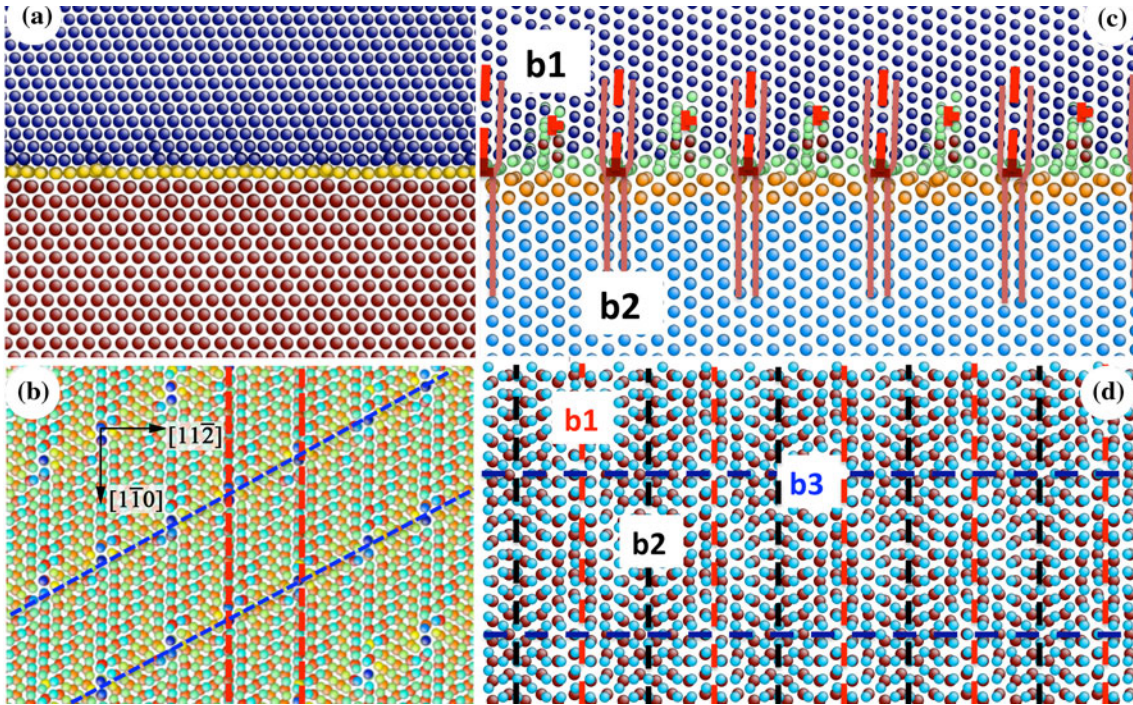


Fig. 4. (a) Transverse view of the relaxed equilibrium structure of the $\{111\}\text{Cu}||\{110\}\text{Nb}$ KS interface, (b) plan view of this interface to expose the misfit dislocation pattern, (c) transverse view of the relaxed equilibrium structure of the $\{112\}\text{Cu}||\{112\}\text{Nb}$ KS interface, and (d) plan view of this interface to show the interfacial dislocation network. The methods used to characterize these dislocations can be found in Ref. 22.

in-plane Burgers vector of $\mathbf{b}_2 = \mathbf{b}_{\text{In}} = a_{\text{Cu}}[111]/3$, a Frank partial, and the spacing is 18.7 Å. The last set has an in-plane Burgers vector of $\mathbf{b}_3 = a_{\text{Cu}}[110]/2$ with spacing 24.8 Å, and it is visible in Fig. 4d.

In contrast, the $\{111\}\text{fcc}||\{110\}\text{bcc}$ KS interface is atomically flat, not faceted. Both the $\{111\}$ plane in Cu and the $\{110\}$ plane in Nb associated with the $\{111\}\text{fcc}||\{110\}\text{bcc}$ KS interface are planes of high atomic density and are atomically flat. The $\{111\}\text{fcc}||\{110\}\text{bcc}$ KS interface contains two sets of interfacial dislocations, as indicated in its plan view in Fig. 4c. Both sets of misfit dislocations have in-plane Burgers vectors. When expressed in the $x = [11\bar{2}]\text{fcc}||[112]\text{bcc}$, $y = [111]\text{fcc}||[110]\text{bcc}$, and $z = [1\bar{1}0]\text{fcc}||[111]\text{bcc}$ coordinate system, one array is oriented parallel to $[001]$ within the interface with Burgers vector $[-2.45 \ 0 \ 1.56]$ with spacing 21.5 Å and the other lies along $[0.88 \ 0 \ 0.47]$ with Burgers vector $[0 \ 0 \ 2.70]$ and spacing 12.3 Å.

ENERGY AND KINETICS

Interfacial Energy

The interface formation energy is associated with the creation of the equilibrium interface structures discussed in the previous section. MD calculations find that the formation energy of the $\{112\}\text{Cu}||\{112\}\text{Nb}$ KS interface ranges from $\sim 820 \text{ mJ/m}^2$ to 886 mJ/m^2 .^{19,20} The formation of the secondary $\{110\}\langle 001\rangle\text{Cu}||\{112\}\langle 110\rangle\text{Nb}$ interface

generated in ARB is higher, $\sim 950 \text{ mJ/m}^2$. In comparison, the atomically flat $\{111\}\text{Cu}||\{110\}\text{Nb}$ KS interface is known to be much lower in formation energy ($\sim 580 \text{ mJ/m}^2$).²¹ Thus the creation of the high-energy $\{112\}\text{Cu}||\{112\}\text{Nb}$ KS interface over the low-energy $\{111\}\text{Cu}||\{110\}\text{Nb}$ KS interface in extreme strain rolling cannot be explained completely by interfacial energetics alone. Using the same methods, we find that the interfacial formation energy of the $\{110\}\text{Cu}||\{111\}\text{Nb}$ $\langle 111\rangle\text{Cu}||\langle 110\rangle\text{Nb}$ interface that hypothetically would result as a consequence of matching a theoretical Cu rolling texture with a theoretical Nb rolling texture is much higher (greater than 1100 mJ/m^2). This is the first indication as to why the interface associated with stable rolling textures of monolithic Cu and Nb is not predominant in ARB nanocomposites, and the texture of nanocomposites (discussed later) deviates significantly from the expected Cu or Nb texture as the interfacial density increases.¹³

Interfacial Shear

In a series of recent works,^{19,22,23} the response of interfaces to simple shear applied parallel to the interface plane was studied using MD simulation, and interface shear strengths were obtained. These results reveal that the shear response is strongly related to interfacial characteristics, such as whether they are flat or stepped in addition to the Burgers vectors of the interface dislocations. The

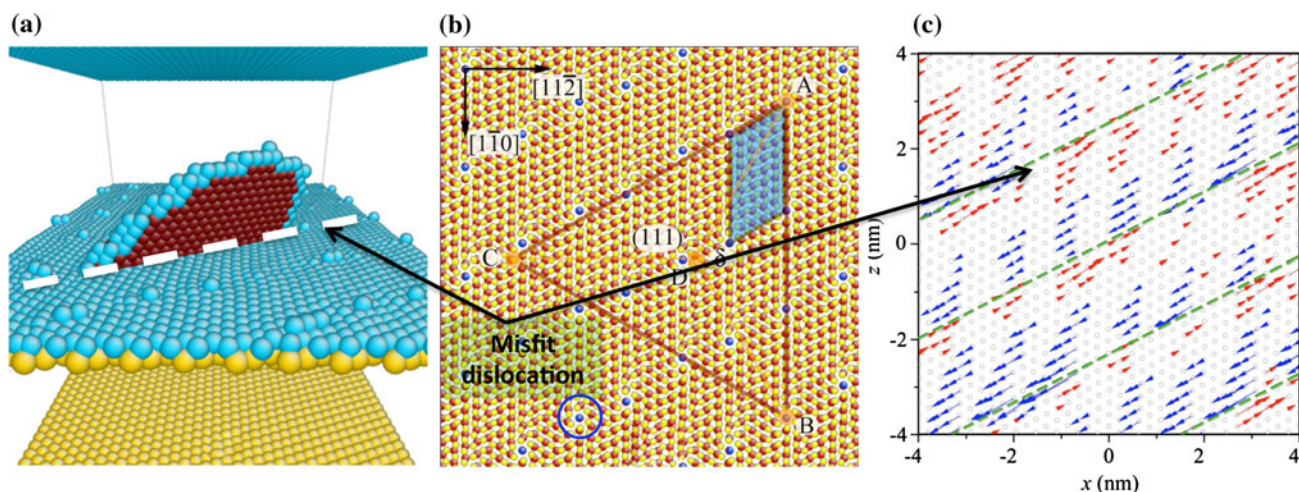


Fig. 5. (a) Nucleation of a single Shockley partial dislocation loop when the bi-crystal model is subjected to in-plane tension. This loop was induced by stress concentrations in the interface generated around a misfit under the applied strain state, (b) plan view of the interface showing the intersection lines formed between three Cu $\{111\}$ slip planes and the (111) plane of the interface, and (c) plan view of the interface showing the relative shear displacement generated in the interface under the applied loading. The shear displacements are resolved about slip plane trace (111) on the interface plane, where the relative shear displacement is defined as the difference between the average shear displacement on the left and right side of a given trace. The arrows indicate the direction of these displacements and the color of the arrows signifies the direction.

$\{111\}\text{Cu}||\{110\}\text{Nb}$ interface responds by interfacial sliding to an applied shear directed along all possible in-plane directions. It has a low shear resistance due to the easy creation and growth of interface dislocation loops at the intersection of misfit dislocations.²³ In contrast, the $\{112\}\text{Cu}||\{112\}\text{Nb}$ interface is highly anisotropic and slides when sheared in some directions with the same mechanism as that in $\{111\}\text{Cu}||\{110\}\text{Nb}$ interface, while it emits dislocations into the Cu crystals when sheared in other directions.^{19,22} Emission occurs by dissociation of misfit dislocations in the interface into Shockley partial dislocations in the Cu crystal. The thresholds for both sliding and emission for the $\{112\}\text{Cu}||\{112\}\text{Nb}$ interface are significantly higher (>1.5 GPa) than that to slide the $\{111\}\text{Cu}||\{110\}\text{Nb}$ interface (less than 0.8 GPa).²³

Dislocation Nucleation

Consider now the interfacial response to other applied stress states, such as uniaxial stresses normal or parallel to the interface, which have no in-plane shear component. Under these conditions, dislocation slip in the adjoining crystals is favored over interfacial sliding. In coarse-grained or ultra-fine-grained materials, dislocations can nucleate either within the crystalline phases, at grain boundaries, and/or the bimetal interface. When the individual layer thicknesses are very fine (tens of nm or less) and grain boundaries are spaced several h apart, it becomes increasingly likely that the dislocations gliding in the phases originate primarily from the bimetal interface. This special case of dislocation nucleation from bimetal interfaces and the effects of interface structure on dislocation

nucleation are studied below using atomic-scale simulations.

There are two ways an interface can supply a lattice dislocation, either production of a new loop via a stress concentration or by splitting (dissociating) a preexisting misfit dislocation into a lattice dislocation and a residual. In the former, the interfacial dislocations retain their Burgers vector, but in the latter, the misfit Burgers vector is altered. The perfect $\{111\}\text{fcc}||\{110\}\text{bcc}$ KS interface contains misfits with only in-plane Burgers vectors, and thus, it can only supply lattice dislocations via stress concentration (Fig. 5a). The perfect stepped $\{112\}\text{fcc}||\{112\}\text{bcc}$ KS interface contains misfits with both in-plane and out-of-plane components, and thus, it can potentially dissociate (under an appropriate stress) into a lattice dislocation. Consequently, the two interfaces, the $\{111\}\text{fcc}||\{110\}\text{bcc}$ KS PVD interface and $\{112\}\text{fcc}||\{112\}\text{bcc}$ KS ARB interface, would nucleate dislocations by entirely different mechanisms, which would naturally have different activation barriers (critical resolved shear stresses) for dislocation nucleation and different dislocation nucleation rates.

In the example of the flat PVD KS interface, the shear strain localizes about the misfit dislocations in the interface when an in-plane strain is first applied. Lattice dislocation nucleation as seen in Fig. 5a occurs to relieve the stress concentrations. Figure 5c presents the map of relative shear displacement in the interface for the case of x -axis straining of a KS interface shown in Fig. 5a. The maximum relative shear occurs along the intersection line where the slip plane (111) intersects the interface (Fig. 5b). This localized elastic shearing occurs in the first steps of loading and as the applied

load increases further, it drives the nucleation and expansion of a dislocation loop with Burgers vector $[\bar{1}21]$ on the slip plane $(1\bar{1}\bar{1})$. It should be mentioned that loops are not produced on other slip systems that have the same Schmid factor under this loading since they would not as effectively relieve the stress concentration.²⁴ To create the same size loop ($\sim 11 \text{ nm}^2$), the energy to nucleate a loop from the KS interface ($\sim 2 \text{ eV}$)²⁵ is significantly lower than homogeneous nucleation within a perfect single crystal of Cu (16 eV to 24 eV).²⁶ In addition, the same mechanism applies to the NW orientation relationship. The significant difference is that in the NW interface, the same applied strain state activates two slip systems instead of one, since the misfit network of the NW interface produces shear stress concentrations in regions where two slip planes intersect the interface.

Nucleation of dislocations from stepped $\{112\}\text{fcc}||\{112\}\text{bcc}$ KS interfaces proceeds via a different mechanism, involving the dissociation of interface dislocations.²⁷ A detailed description of the mechanism and how it dictates slip system selection under different loading states is given in Wang et al.,²² in this issue.

In summary, the atomic structure of the interface dictates where in the interface dislocations nucleate, the slip system(s) on which they nucleate, and how they nucleate. The threshold for nucleating dislocations by dissociation of a misfit is expected to be lower than that to form a new Shockley dislocation by the stress concentration generated by a misfit within the flat interface. Thus, compared to flat interfaces, stepped interfaces appear to be more effective sources for dislocations. As will be discussed shortly, this notion is confirmed through our large-scale atomistic simulation of shock compression of nanolayered composites.²⁷

Dislocation Transmission

In the previous sections, we have seen the responses of interfaces to an applied load. An applied load can also generate lattice dislocations that can interact with the interface. The structural details of a given interface can influence whether dislocations can transmit across the interface, pile-up at the interface, become absorbed within the interface, reflect from the interface, or annihilate at the interface. As an example of dislocation/interface interactions, we consider dislocation transmission. When the individual layer thickness reduces to a few tens of nanometers and below, dislocation nucleation and propagation within the bulk, even as gliding hairpin loops, becomes energetically unfavorable compared to dislocation transmission across the interface.²⁸ Thus, dislocation transmission becomes important for supporting continued plasticity.

Two aspects are important for transmission. First, there is the geometric aspect. Slip systems of

a crystal on one side of the interface have to be well aligned with slip systems of the crystal on the other side of the interface. A pair of fcc/bcc slip systems is considered to provide a geometrically efficient pathway for transmission when their Burgers vectors are aligned and their slip planes are joined at the interface. If we let κ be the minimum angle between their Burgers vector and θ the minimum angle between the intersection lines that each plane makes with the interface, then an fcc/bcc pair that provides an efficient transmission pathway would have a value of

$$\chi = \cos\left(\frac{\pi}{2}\frac{\theta}{\theta_c}\right) \cos\left(\frac{\pi}{2}\frac{\kappa}{\kappa_c}\right) \quad (1)$$

equal to or close to unity,²⁹ where the angles θ_c and κ_c are the limiting angles for κ and θ , respectively. According to Eq. 1, when either κ or θ exceeds their corresponding thresholds, transmission is not possible. The χ measure in Eq. 1 is independent of the applied stress state. The Schmid factor of the outgoing slip system m_{OUT} has been shown to be important,³⁰ which would lead to a modification of Eq. 1 to $\chi_\sigma = \chi m_{\text{OUT}}$. Second, the activation barrier for transmission must be low. Interfaces that are weak in shear are difficult for dislocations to cross. An approaching dislocation tends to dissipate energy by shearing the weak interface ahead of it. Upon impinging the interface, the dislocation gets absorbed and spreads in the interface rather than crossing it. Interfaces that are stronger in shear are much easier for a dislocation to cross due to the reduced core spreading that occurs as the dislocation enters the interface.

Both the geometrical and energetic aspects are important. An interface may have many fcc/bcc slip system pairs that offer geometrically efficient pathways for transmission, but if it is at the same time weak in shear, then it will present a large barrier to transmission. On the other hand, an interface may have few efficient transmission pathways, but if it is resistant to sliding, then it will support dislocation transmission. The PVD interface $\{111\}\text{fcc}||\{110\}\text{bcc}$ is an excellent example of the former. The fcc and bcc crystals are oriented such that there are 15 distinct geometrically efficient pathways (with $\chi > 0.9$), as indicated on Table I. (In Table I, critical angles θ_c and κ_c are set to 15° and 45° , respectively.) Despite this, because it has a relatively low shear resistance,²³ it is energetically favorable for approaching dislocations to become absorbed into the interface rather than transmit across it.³¹ In this case, transmission becomes a thermally activated process.³² After the incoming dislocation becomes absorbed and extended within the plane of the interface, in order for it to transmit into the other crystal, it must then “renucleate” and bow out onto the outgoing slip system, an event that is aided by thermal activation. The ARB $\{112\}\text{fcc}||\{112\}\text{bcc}$ interface, in contrast, is more

Table I. Number of dislocation transmission pathways for three interfaces with a KS orientation relationship

Transmission factor	PVD $\{111\}fcc\ \{110\}bcc$ $\langle 112 \rangle fcc \ \langle 112 \rangle bcc \ \text{RD}$	ARB $\{112\}fcc\ \{112\}bcc$ $\langle 111 \rangle fcc \ \langle 110 \rangle bcc \ \text{RD}$	Theoretical rolling $\{110\}fcc\ \{111\}bcc$ $\langle 111 \rangle fcc \ \langle 111 \rangle bcc \ \text{RD}$
χ in Eq. 1	15	18	7
χ_σ from Cu to Nb	6	5	6
χ_σ from Nb to Cu	5	6	2

Column 1: with $\{111\}Cu\|\{110\}Nb$ interface planes (characteristic of PVD foils), column 2: interface planes (characteristic of ARB composites), and column 3: interface planes (which would manifest from randomly pairing theoretical textures). The number of distinct pathways satisfying $\chi > 0.9$ and $\chi_\sigma > 0.2$ are given

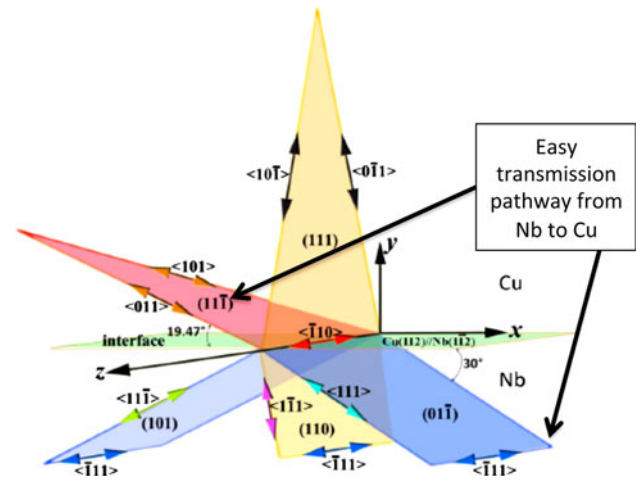


Fig. 6. The $\{112\}||\{112\}$ interface. The upper Cu crystal with two of its four slip planes drawn is connected to the lower Nb crystal across the interface plane (green plane). These two $\{111\}$ planes intersect the interface along (110) , the line orientation of the two misfit dislocations b_1 and b_2 in the interface (Fig. 4c). Here we indicate a pair of fcc and bcc slip systems, $(111)fcc-(011)bcc$, where the dislocation transmission pathway is geometrically efficient.

amenable for dislocation transmission, particularly under rolling. It contains the highest number of potential transmission fcc/bcc pairs, and it is much more resistant to shearing (Fig. 4c), which favors transmission. Calculation of χ in Eq. 1 reveals that one fcc/bcc slip system, in particular, has a large χ . This special pair is illustrated in Fig. 6. As we shall see in subsequent MD simulations, the enhanced ability of the $\{112\}fcc\|\{112\}bcc$ KS interface to transmit dislocations affects its texture evolution, plastic response to shock loading, and its propensity to twin. The number of possible transmission pathways for the $\{110\}Cu\|\{111\}Nb$ $\langle 111 \rangle Cu\|\langle 110 \rangle Nb$ interface, associated with the theoretical rolling texture, is the lowest among the three in Table I, an aspect that provides another explanation as to why this interface is not observed in ARB nanocomposites.

The ability of an interface to transmit dislocations may change with strain. Over the duration of plastic deformation, the interface must interact with a high flux of dislocations. These dislocations either become stored in the interface or transmit across it. Even if they were to transmit, residual dislocations are deposited in the interface since the Burgers vectors of the incoming and outgoing dislocations are unequal. Thus either way, dislocation/interface interactions can increase the extrinsic dislocation density stored in the interface with applied strain. In the event that this extrinsic density is not recovered, it can affect the ability of the interface to transmit subsequent dislocations. It can be envisioned that this density could, on the one hand, repel subsequent dislocations, thereby hindering transmission, or on the other hand, it can increase the interfacial shear strength, thereby promoting

transmission with strain. For the PVD multilayers with $\{111\}\text{fcc}||\{110\}\text{bcc}$ interfaces, transmission is suspected to occur when the individual layer thickness decreases below 5 nm,²⁸ whereas for the ARB multilayers, transmission is deduced to happen below 50 nm.^{11,13,14}

Recovery

In order for the interface to remain stable under deformation or other extreme environments, it must be able to store and recover from numerous interactions with defects. Accumulated defects can reassemble and reemit into the adjoining crystals³³ or annihilate within the interface. At the heart of these mechanisms lies the ability of defects to migrate or move within the interface. The same defect may find it easier to move in one interface than another by virtue of interface structure. Interfaces that possess the structural qualities to support defect transport and the “right” kinetics are referred to as being *kinetically stable*. Modeling dislocation recovery processes in the interface is an unexplored, yet important area.

For PVD KS interfaces, dislocation recovery within interface is apparently efficient. It has been observed that the interface remains sharp and flat after 75% rolling reduction. Atomistic simulations suggest that recovery is aided by the ease with which dislocations can climb and glide within the interface. Climb is facilitated by the high diffusivity of vacancies, and easy glide is attributed to the low shear resistance characteristics of this interface.³⁴

For the ARB $\{112\}\text{fcc}||\{112\}\text{bcc}$ interface, recent studies suggest that it has the ability to recover from accumulation of extrinsic defects generated during extreme plastic straining. We analyzed the defect structure of both the relaxed equilibrium structure predicted by MD and the actual Cu/Nb interface found in an ARB sample that experiences over 1000% strain. Remarkably, we find that the Cu/Nb interface (Fig. 3c), despite having been exposed to high fluxes of dislocations, resembles that predicted by MD for an undeformed Cu/Nb interface (Fig. 4c). This seemingly defect-free interface may lead one to infer that this interface structure facilitates self-healing mechanisms, an attribute that would, at least partly, explain why it is stable after >1000% strain.

INTERFACE-DRIVEN RESPONSE

Differences in the ability of the two interfaces to emit lattice dislocations and transmit dislocations will greatly impact composite material response, particularly as the distance between two adjacent bimetal interfaces reduces down to the nanoscale. To illustrate, we examine the effects of interface structure on texture evolution, shock compression response, and the propensity for deformation twinning.

Texture Evolution

Texture is the distribution of crystal orientation. It is well known that deformation processing, such as rolling or extrusion, causes substantial changes in texture and greatly influences the deformation response of the material.^{13,35–38} Texture evolution depends on the fabrication process. When multilayered Cu-Nb composites are pushed to extreme plastic strains in ARB processing, we observed a unique texture development as a function of decreasing layer thickness.¹³ An analysis of texture measurements by neutron diffraction (Fig. 7a) and EBSD of the $h = 18$ nm ARB composites, for instance, reveals that they are unlike the rolling textures of those of severely deformed monolithic Cu or Nb (Fig. 7b). Specifically, the Cu phase contains a predominance of Copper $\{112\}\langle 111\rangle$ and Goss $\{110\}\langle 001\rangle$ components and lacks the Brass component. The Nb phase is dominated by a near $\{112\}\langle 110\rangle$ component in the α fiber. They are also unlike those seen in PVD (Fig. 7c) and wire drawing.^{10,37,38}

The texture analysis agrees with the evolution towards two predominant interfaces $\{112\}\text{Cu}||\{112\}\text{Nb}$ $\langle 111\rangle\text{Cu}||\langle 110\rangle\text{Nb}$ and $\{110\}\text{Cu}||\{112\}\text{Nb}$ $\langle 001\rangle\text{Cu}||\langle 110\rangle\text{Nb}$ formed in ARB composites. Figure 8 illustrates the orientation relationship between a Cu crystal and Nb crystal joined at an interface, when the orientations are expressed as rolling components in the standard convention of the rolling plane normal and RD: $\{\text{ND}\}\langle \text{RD}\rangle$. For nanolayered composites, the layers are one grain thick, and so all grains are bounded by Cu-Nb interfaces. Joining single crystals of one of either of the dominant components of the Cu (Copper $\{112\}\langle 111\rangle$ and Goss $\{110\}\langle 001\rangle$) with that $\{112\}\langle 110\rangle$ of Nb creates the two prevailing interfaces of ARB. This result clearly demonstrates that evolution towards preferred bimetal interfaces with extreme rolling strain governs texture evolution.

We find via polycrystal calculation that this particular Cu texture arises from planar slip, described as slip occurring by slip systems acting on the same plane (Fig. 9). As the layer thickness reduces, dislocation transmission becomes a viable source for dislocations that tend to glide on those planes where dislocation transmission is easiest. Planar slip is likely promoted on the $(11\bar{1})$ slip plane shown in Fig. 6, which illustrates one transmission pathway from Nb to Cu that will likely be preferred as it has a high χ and a high outgoing resolved shear stress under rolling. (The texture in Fig. 9b was achieved via planar slip and therefore is unstable; if planar slip continues, then the texture will continue to evolve under further rolling strains and reductions in layer thickness until a more symmetric slip orientation is achieved.)

Shock

Next, we compare the shock compression response of Cu-Nb nanolayer composites with two

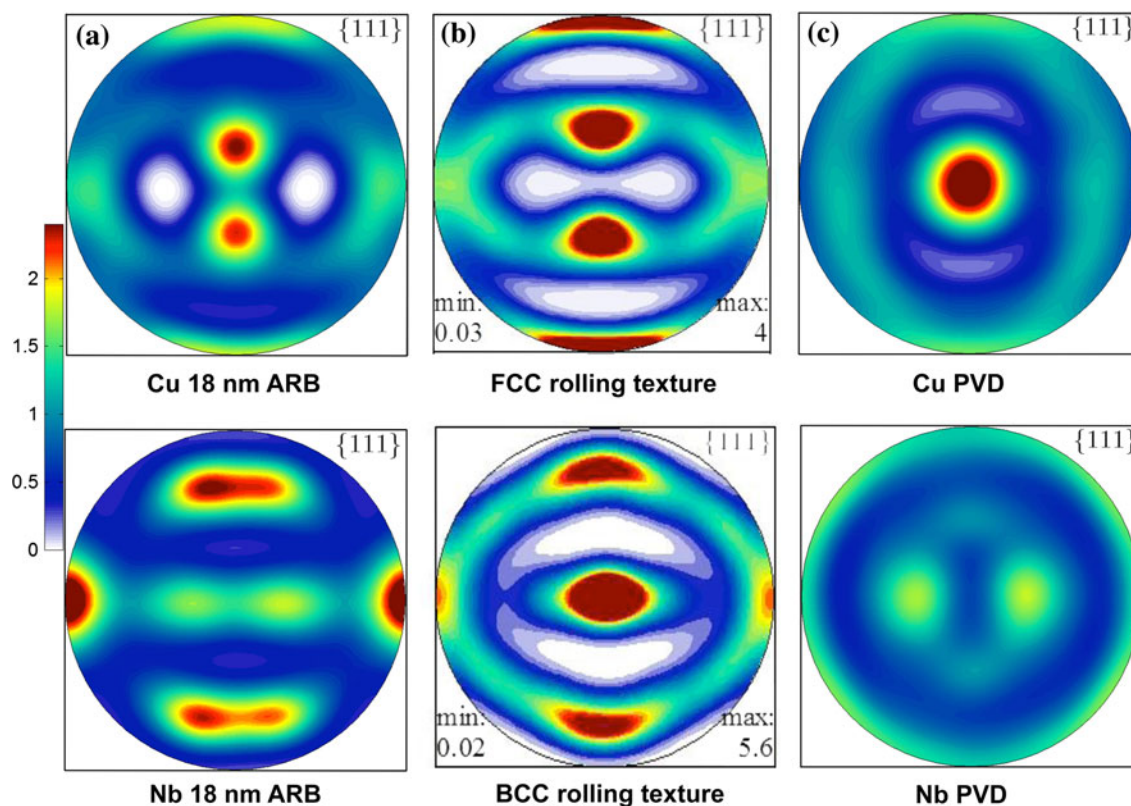


Fig. 7. $\{111\}$ pole figures of (a) measured ARB Cu-Nb texture for $h = 18$ nm. ODFs and fiber plots of these textures can be found in Ref. 13. (b) conventional slip-dominated rolling texture in fcc and bcc and (c) measured PVD Cu-Nb texture. ODFs and fiber plots of the latter can be found in Ref. 13.

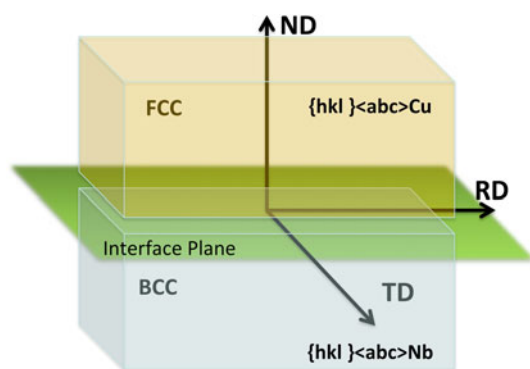


Fig. 8. Schematic of the orientation relationship between a Cu crystal and a Nb crystal joined at an interface in which the orientations are expressed as rolling components.

different interface structures using large-scale atomic simulation. The results clearly demonstrate that faceted $\{112\}\text{Cu}||\{112\}\text{Nb}$ interfaces are better sources for dislocations nucleation and have weaker barriers to dislocation transmission than the $\{111\}\text{Cu}||\{110\}\text{Nb}$ interface. As shown in Fig. 10, an atomistic model of a multilayered composite was constructed of alternating single crystals of two dissimilar metals forming several bimetal interfaces, lying parallel to the x - y plane. The nonequilibrium

MD simulations of shock loading utilize the scalable parallel short-range molecular dynamics (SPaSM) code with shock waves induced by pushing the sample against a specularly reflecting wall at a piston velocity of u_p . The shock direction corresponds to the z -direction in Fig. 10, directed normal to the interfaces. It is worth mentioning that the interatomic potential for Cu is Voter–Chen³⁹ and a Finnis–Sinclair (FS) potential by Ackland and Thetford for Nb.⁴⁰ In particular, among six existing Nb potentials, we found that the Ackland’s FS potential was one of two that could reasonably reproduce the stacking fault under high pressure as predicted by using first-principle calculation.⁴¹

With these potentials, multilayer models are first constructed with either the flat $\{111\}\text{Cu}||\{110\}\text{Nb}$ KS or faceted $\{112\}\text{Cu}||\{112\}\text{Nb}$ KS interface. The interface spacing is 5 nm and the composite model contains 23 bimetal interfaces. The flat KS multilayer material is 129.64 nm long, containing 3,210,192 atoms. The faceted KS material is 121.81 nm long with 3,018,720 atoms.

Shock loading imposes uniaxial strain, which generates a three-dimensional stress state (e.g., Ref. 42). As the shock compression wave propagates across the sample, a high deviatoric internal stress develops in the vicinity of the interfaces. The response is elastic until the onset of plasticity at a

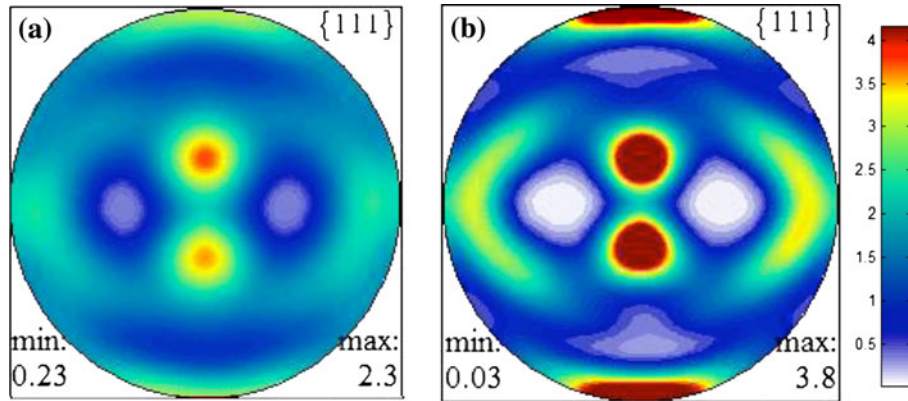


Fig. 9. Comparison of the $\{111\}$ pole figures for the Cu phase in the ARB composite (a) measured and (b) calculated assuming planar slip. The main components are similar but the predicted texture is overall more intense. It is common that polycrystal calculations predict more intense deformation textures than measured.

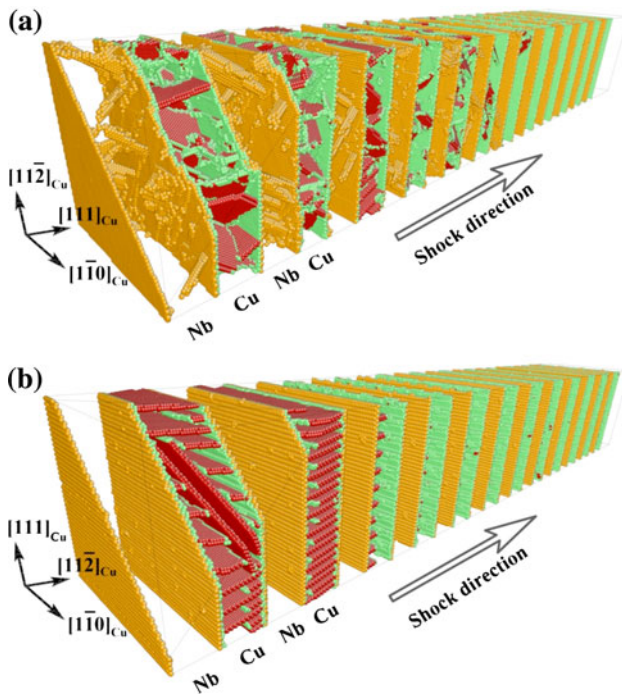


Fig. 10. MD simulations of shock compression of Cu-Nb multilayers with $h = 5$ nm thick layers and (a) $\{111\}\text{Cu}||\{110\}\text{Nb}$ KS interfaces and (b) $\{112\}\text{Cu}||\{112\}\text{Nb}$ KS interfaces.

certain threshold speed. In both cases, plasticity in the Cu phase is due to dislocation nucleation from the interface and plasticity in the Nb phase is due to transmission of Cu into Nb. However, due to the ease at which the $\{112\}\text{Cu}||\{112\}\text{Nb}$ interface nucleates and transmits dislocations compared to the $\{111\}\text{Cu}||\{110\}\text{Nb}$ interface, the two interfaces result in significantly different changes in the shock response of the parent multilayer composite. First, the simulations find that for the $\{112\}\text{Cu}||\{112\}\text{Nb}$ interface, the threshold for nucleating Shockley partials in Cu is less than that to transmit partials from Cu to Nb, whereas for the $\{111\}\text{Cu}||\{110\}\text{Nb}$

interface, the barriers for these two events were comparable. In the former, Shockley partial dislocations emit from the interface via dissociation of interfacial misfit dislocations onto two $\{111\}$ planes. Slip by continual partial emission remains confined to the Cu layers until the piston speed is increased such that these dislocations can transmit into Nb. In the $\{111\}\text{Cu}||\{110\}\text{Nb}$ interface, on the other hand, Shockley leading partials then trailing partials are emitted on predominantly one slip system. The full dislocations then transmit straight into Nb. Afterwards, multislip plasticity in both the Cu and Nb phases ensues. Second, the piston speed at which dislocations nucleate (350 m/s) and transmit (500 m/s) across the $\{112\}\text{Cu}||\{112\}\text{Nb}$ interface is much lower than that for the $\{111\}\text{Cu}||\{110\}\text{Nb}$ interface (650 m/s).

These simulations confirm undoubtedly that by virtue of differences in atomic structure between the atomically flat interface and atomically stepped interface, the multilayer nanocomposite changes significantly when and on which slip systems dislocations first nucleate and when and on which slip systems they transmit.

Twinning

Like dislocation slip, twinning is another important mechanism governing material deformation behavior. It is known that severe plastic deformation and fine (nm)-grained materials together can promote deformation twinning^{43,44} in metals that would not twin under moderate strain conditions in coarse-grained materials. However, in multilayered composites, large stress states and ultrafine scales are not the only factor controlling deformation twinning. Another factor, the bimetal interface, can have a profound effect on deformation twinning. A dedicated discussion on interface-facilitated twinning in Cu-Ag composites is given in the article by Mara et al.⁴⁴ in this issue. Here, we continue with our Cu-Nb example. We have already learned

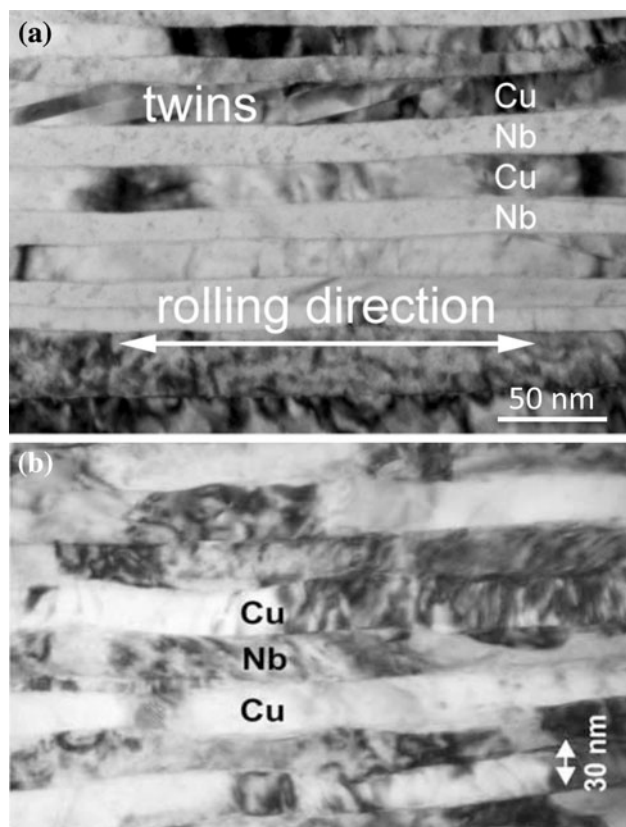


Fig. 11. TEM micrographs showing rolled (a) ARB Cu-Nb nanolayers with twins in the Cu phase and (b) PVD Cu-Nb nanolayers with no twins.

that the $\{112\}fcc\|\{112\}bcc$ interface nucleates Shockley partials and transmits dislocations more easily than the $\{111\}fcc\|\{110\}bcc$ interface. As we discuss below, it turns out that these fundamental differences enable the $\{112\}fcc\|\{112\}bcc$ interface to promote profuse twinning and the $\{111\}fcc\|\{110\}bcc$ interface to completely suppress it.

Recent experimental studies have demonstrated that under the same length scale and the same rolling conditions, nanoscaled Cu-Nb multilayer composites synthesized by PVD and by ARB exhibit dramatically different twinning propensities. From the former interface, deformation twinning did not initiate in shock, nanoindentation, and when rolling, reducing the individual layer thickness from 75 nm to 30 nm (Fig. 11b).^{4,45,46} However, from the latter interface, deformation twins formed in the Cu layer in shock, nanoindentation, and in rolling when the individual layer thicknesses reduced below 50 nm (Fig. 11a). The twin fraction increased continually as the layer thickness reduced to 10 nm.^{5,12,13}

To explain deformation twinning, we first need to identify the source for twinning partials. All twins observed in the ARB composites were connected to $\{112\}Cu\|\{112\}Nb$ KS interfaces and formed on the $\{111\}$ plane that lies $\sim 19.5^\circ$ from the interface plane¹¹ (Fig. 12). This twinning plane is special in

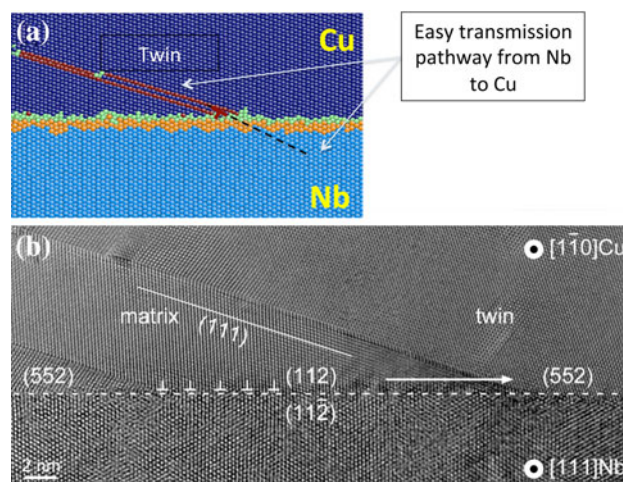


Fig. 12. (a) MD simulation showing nucleation of a Cu deformation twin from a $\{112\}Cu\|\{112\}Nb$ KS interface that was triggered by a Nb full dislocation impinging on the interface and transmitting across the interface as two twinning partials in Cu. (b) HRTEM micrograph showing a typical deformation twin emanating from the $\{112\}Cu\|\{112\}Nb$ KS interface in an ARB composite. The twin has transformed the interface to $\{552\}Cu\|\{112\}Nb$.

two ways: it intersects the interface along a line that is parallel to the line orientation of the misfit dislocations in the interface and it is well aligned with a $\{110\}$ slip plane in Nb (Fig. 6). The first feature implies that a twinning partial could be supplied by dissociation of a misfit dislocation, and the second feature indicates that a twinning partial could also be provided by a transmission of a Nb dislocation into Cu. These notions led Han et al.¹¹ to postulate that twin nucleation from $\{112\}fcc\|\{112\}bcc$ KS interfaces occurred either via dislocation transmission or dissociation of misfit dislocations, or a combination of both. As neither mechanism is easy in the $\{111\}fcc\|\{110\}bcc$ KS interface, this would explain why twins do not form in the PVD nanocomposites, even at extreme nanoscales and in extreme deformation conditions.

MD simulations were carried out in which a full Nb dislocation was driven towards the $\{112\}Cu\|\{112\}Nb$ KS interface. As the Nb approached the interface, its stress field caused the misfit to dissociate into a Shockley partial. Upon reaching the interface, it transmits across it into Cu as a second Shockley partial, gliding on a plane adjacent to the first partial. This MD calculation confirms that this $\{112\}Cu\|\{112\}Nb$ KS interface can act as a source for twins, wherein a twin nucleus is formed by both misfit dissociation and dislocation transmission (Fig. 12). The MD simulation in Fig. 12a presents one possible kinetic pathway for twin nucleation; others are of course possible, but they will likely involve either dislocation transmission or misfit dissociation.

Second, we need to explain twin growth after nucleation. Two growth mechanisms have been

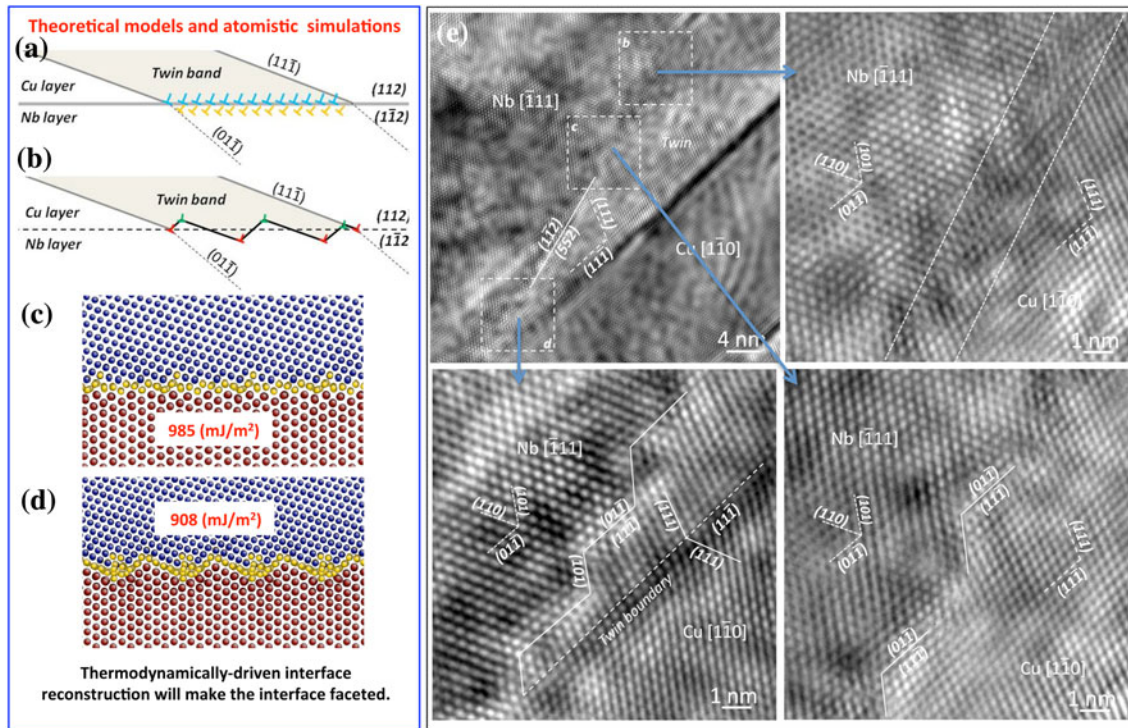


Fig. 13. Growth mechanisms of twins in Cu. (a) Twinning by sequential slip transmission from Nb to Cu, leaving an array of residual dislocations in the interface, (b) reconstruction of residual dislocations within the interface, (c) and (d) MD simulations of interfaces (c) immediately after twinning, and (d) after rearrangement to a low energy state and (e) HRTEM images show interface structure after twinning.¹¹

proposed based on observations from TEM.^{11,12} The first involves sequential transmission of Nb dislocations to Cu twinning partials on adjacent planes in Cu.¹¹ Each transmission event would leave a residual behind (Fig. 13a). As deposited, this fine array of residuals would leave the interface in a disordered state. Driven to achieve a lower energy state, they, in time, can coalesce to an ordered state, different than the original one prior to twinning (Fig. 13b). Evidence of this evolution is seen in postmortem TEM of a single-twin interface (Fig. 13e). A possible reconstruction of the interface after this twinning process is calculated by MD simulation (Fig. 13c, d). Before reconstruction, the interface contains a nonuniform array of facets as a result of sequential transmission (Fig. 13c) and leaves the interface in a high-energy state. After reconstruction, the new interface is ordered, with broader facets and lower formation energy (Fig. 13d). Both interfaces in Fig. 13c, d have the same net Burgers vector and satisfy the orientation relationship and interface plane expected of the newly twinned Cu/Nb interface; however, the lower energy one in Fig. 13d best agrees with the final twinned interface observed in the sample Fig. 13e. The second growth mechanism is the alternating emission mechanism proposed in Ref. 12 that was observed in in-situ nanoindentation in the TEM. In this mechanism, twins expand by twinning partial emission from both boundaries bordering a given layer.

This single example demonstrates how interface structure can potentially control the relative activities of slip and twinning. The $\{112\}\text{Cu}||\{112\}\text{Nb}$ KS interface favors twinning by virtue of its effective dislocation nucleation and transmission properties. In contrast, the $\{111\}\text{Cu}||\{110\}\text{Nb}$ KS interface in the PVD multilayers is weak in shear, posing an enormous barrier for transmission, and contains an intrinsic dislocation network with Burgers vectors with no out-of-plane components.

ARB COMPOSITE PROPERTIES

As the ARB nanocomposites were prepared in the form of bulk sheet, there is little limit on the kinds of experimental tests one can perform. They, like the Cu-Nb nanocomposites prepared by PVD, also possess many outstanding properties. They are several times stronger than Cu or Nb alone. Figure 14a compares the tensile response of the ARB composites in the RD direction with the compression stress-strain curves for PVD foils from micropillar compression tests.³ As shown, the ARB material achieves peak strength at approximately 1 GPa. Differences in their deformation responses between the PVD and ARB material can be attributed to several factors, such as differences in texture and interface properties, to name a few. As shown in Fig. 14b, these composites possess hardness values several times that of its constituents.

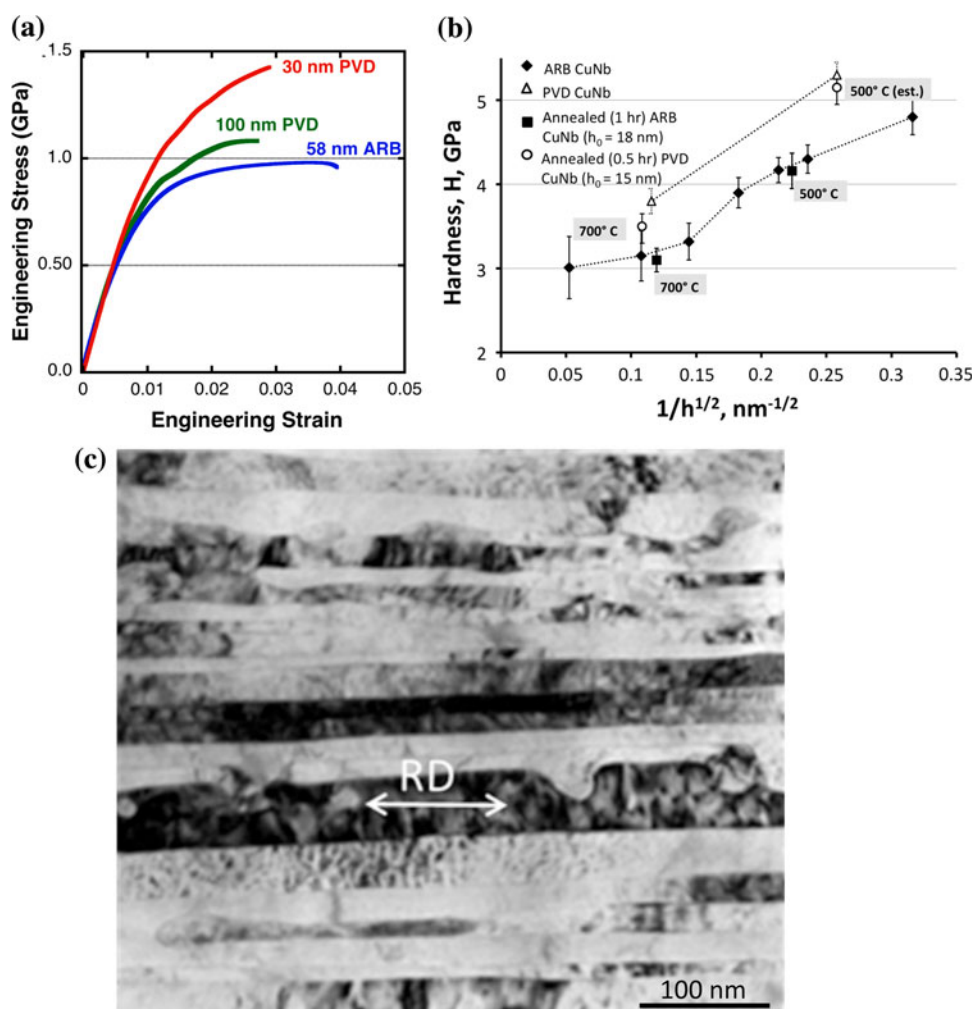


Fig. 14. (a) Stress–strain curves for Cu-Nb nanolayered composites fabricated by PVD ($h = 100$ nm and 30 nm³) and by ARB ($h = 58$ nm). (b) Hardness of the Cu-Nb nanolayered composites fabricated by PVD¹ and ARB. The hardness values of the ARB composite after exposure to 500°C and 700°C at 1 h are also shown. (c) Microstructure of the ARB Cu-Nb nanolayered composite after exposure to 500°C for 1 h.

For a wide range of layer thicknesses, the hardness of the ARB composites is found consistently lower than that of the PVD nanocomposites.¹ The constant difference, including even the coarser layers, suggests that differences may be attributed to basic texture differences between the composites (Fig. 7). Last, we mention that the ARB composites also exhibit exceptional thermal stability.⁴⁷ Cu-Nb ARB composites with submicron-layer thicknesses (200–600 nm) did not recrystallize but retained their rolling texture after exposure to elevated temperatures (up to 800°C) for 0.5 h.⁴⁷ Stability is harder to achieve in finer layers. We find that even for ARB composites with $h = 18$ nm layers, the texture and microstructure are retained up to 500°C. Figure 14c presents the microstructure of the $h = 18$ ARB material after heating to 500°C for 1 h. Afterwards, the hardness is nearly unaffected, and the slight drop exhibited is not statistically significant (Fig. 14b).

INTERFACE DESIGN

The new and important result that arises from the recent series of papers on model multilayered nanocomposites is that they can be fabricated via severe plastic deformation (ARB) with well-defined, ordered interface structures that prevail uniformly over the entire composite. Their creation opens the way to probing the nature of interfacial response in mechanical deformation (straining and shock) and interface/defect interactions. The nanocomposites themselves possess many desirable properties, such as ultrahigh strength, hardness, and thermal stability, vastly superior to those of the individual constituents. There is little limit to the number of macroscopic properties that can be characterized with these bulk composites, and more testing is underway.

It is not yet known why the Cu-Nb interfaces self-organized to the ordered $\{112\}\text{fcc}||\{112\}\text{bcc}$ KS

structure under extreme strains. Undoubtedly, the stability of this Cu-Nb structure is tied to the dominance of this interface in plasticity as the interfacial density increases. To rationalize this, three aspects should be considered in tandem: geometry, energetics, and kinetics (see Fig. 2b); considering just one alone does not provide an explanation. For instance, interface formation energy is important, but it is not the only factor that needs to be considered. While this $\{112\}\text{fcc}||\{112\}\text{bcc}$ ARB-interface does not correspond to the energetically lowest $\{111\}\text{fcc}||\{110\}\text{bcc}$ KS interface,²¹ it is also not the interface structure that would be associated with theoretical rolling textures of monolithic Cu or Nb,¹⁰ which has a relatively high formation energy. As a result, as the interfacial density increases, the bulk texture deviates from the expected rolling textures and takes on a texture associated with the $\{112\}\text{fcc}||\{112\}\text{bcc}$ KS and $\{110\}\text{fcc}||\{112\}\text{bcc}$ interfaces. The preference for the $\{112\}\text{fcc}||\{112\}\text{bcc}$ can be understood by also considering dislocation kinetics—when, how, and on what slip systems dislocations glide. As the spacing between adjacent interfaces shrinks, the available sources for dislocations become exclusively located in the interface. Consequently the interface dictates the choice of slip systems on which dislocations move. The activation barriers for dislocation nucleation and dislocation transmission from the $\{112\}\text{fcc}||\{112\}\text{bcc}$ interface are substantially reduced compared to that of the other interfaces. Also, the number of geometrically efficient pathways for transmission across this interface is large.

The studies presented here have revealed a new area of kinetically driven stable interfaces, interfaces that self-organize under a mechanical drive. Understanding such interfaces opens up the possibility of designing the severe plastic deformation-processing route for target interfacial properties.

ACKNOWLEDGEMENTS

Modeling work by I.J.B., R.F.Z. and K.K. was supported by the Center for Materials at Irradiation and Mechanical Extremes, an Energy Frontier Research Center funded by the U.S. Department of Energy, Office of Science, Office of Basic Energy Sciences under Award Number 2008LANL1026. Modeling and experimental work by N.A.M., J.S.C., S.J.Z., W.Z.H., and J.W. was supported by a Los Alamos National Laboratory (LANL) Directed Research and Development (LDRD) project DR20110029. T.N. was supported by the Department of Defense (DoD) through the National Defense Science & Engineering Graduate Fellowship (NDSEG) Program. Nanomechanical testing for this work was performed at the Center for Integrated Nanotechnologies, a U.S. Department of Energy, Office of Basic Energy Sciences user facility. Los Alamos National Laboratory, an affirmative action equal opportunity employer, is operated by Los

Alamos National Security, LLC, for the National Nuclear Security Administration of the U.S. Department of Energy under contract DE-AC52-06NA25396.

REFERENCES

1. A. Misra and R.G. Hoagland, *J. Mater. Res.* 20, 2046 (2005).
2. B.M. Clemens, H. Kung, and S.A. Barnett, *MRS Bull.* 24, 20 (1999).
3. C.C. Aydiner, D.W. Brown, N.A. Mara, J. Almer, and A. Misra, *Appl. Phys. Lett.* 94, 031906 (2009).
4. N.A. Mara, D. Bhattacharyya, P. Dickerson, R.G. Hoagland, and A. Misra, *Appl. Phys. Lett.* 92, 231901 (2008).
5. W.Z. Han, A. Misra, N.A. Mara, T.C. Germann, J.K. Baldwin, T. Shimada, and S.N. Luo, *Philos. Mag.* 91, 4172 (2011).
6. X. Zhang, N. Li, O. Anderoglu, H. Wang, J.G. Swadener, T. Hochbauer, A. Misra, and R.G. Hoagland, *Nucl. Instrum. Methods B* 261, 1129 (2007).
7. L. Thilly, M. Veron, O. Ludwig, F. Lecouturier, and J.P. Peyrade, *Philos. Mag. A* 82, 925 (2002).
8. V.M. Segal, K.T. Hartwig, and R.E. Goforth, *Mater. Sci. Eng. A* 224, 107 (1997).
9. N. Li, J. Wang, J.Y. Huang, A. Misra, and X. Zhang, *Scr. Mater.* 63, 363 (2010).
10. S.-B. Lee, J.E. LeDonne, S.C.V. Lim, I.J. Beyerlein, and A.D. Rollett, *Acta Mater.* 60, 1747 (2012).
11. W.Z. Han, J.S. Carpenter, J. Wang, I.J. Beyerlein, and N.A. Mara, *Appl. Phys. Lett.* 100, 011911 (2012).
12. S.J. Zheng, I.J. Beyerlein, J. Wang, J.S. Carpenter, W.Z. Han, and N.A. Mara, *Acta Mater.* (2012). doi:[10.1016/j.actamat.2012.07.027](https://doi.org/10.1016/j.actamat.2012.07.027).
13. J.S. Carpenter, S.C. Vogel, J. LeDonne, D.L. Hammon, I.J. Beyerlein, and N.A. Mara, *Acta Mater.* 60, 1576 (2012).
14. J.S. Carpenter, X. Liu, A. Darbal, N.T. Nuhfer, R.J. McCabe, S.C. Vogel, J.E. LeDonne, A.D. Rollett, K. Barmak, I.J. Beyerlein, and N.A. Mara, *Scr. Mater.* 67, 336 (2012).
15. F. Dupouy, E. Snoeck, M.J. Casanove, C. Roucau, J.P. Peyrade, and S. Askenazy, *Scr. Mater.* 34, 1067 (1996).
16. L. Thilly, M. Veron, O. Ludwig, and F. Lecouturier, *Mater. Sci. Eng. A* 309/310, 510 (2001).
17. J.K. Chen, D. Farkas, and W.T. Reynolds Jr., *Acta Mater.* 45, 4415 (1997).
18. J.K. Chen, G. Chen, and W.T. Reynolds Jr., *Philos. Mag. A* 78, 405 (1998).
19. M.J. Demkowicz and L. Thilly, *Acta Mater.* 59, 7744 (2011).
20. K. Kang, J. Wang, and I.J. Beyerlein, *J. Appl. Phys.* 111, 053531 (2012).
21. M.J. Demkowicz, R.G. Hoagland, and J.P. Hirth, *Phys. Rev. Lett.* 100, 2 (2008).
22. J. Wang, K. Kang, R.F. Zhang, S.J. Zheng, I.J. Beyerlein, and N.A. Mara, *JOM* (2012). doi:[10.1007/s11837-012-0429-7](https://doi.org/10.1007/s11837-012-0429-7).
23. J. Wang, R.G. Hoagland, X.Y. Liu, and A. Misra, *Acta Mater.* 59, 3164 (2011).
24. R.F. Zhang, J. Wang, I.J. Beyerlein, A. Misra, and T.C. Germann, *Acta Mater.* 60, 2855 (2012).
25. R.F. Zhang, J. Wang, I.J. Beyerlein, and T.C. Germann, *Scr. Mater.* 65, 1022 (2011).
26. G.S. Xu and A.S. Argon, *Philos. Mag. Lett.* 80, 605 (2000).
27. R.F. Zhang, J. Wang, X.Y. Liu, I.J. Beyerlein, and T.C. Germann (Paper presented at the Proceedings of the 17th APS Topical Conference on Shock Compression of Condensed Matter 1426, 1251, 2012).
28. A. Misra, J.P. Hirth, and R.G. Hoagland, *Acta Mater.* 53, 4817 (2005).
29. E. Werner and W. Prantl, *Acta Metall. Mater.* 38, 533 (1990).
30. T.C. Lee, I.M. Robertson, and H.K. Birnbaum, *Scr. Mater.* 23, 799 (1989).
31. J. Wang, R.G. Hoagland, J.P. Hirth, and A. Misra, *Acta Mater.* 56, 5685 (2008).
32. J. Wang and A. Misra, *Curr. Opin. Solid State Mater. Sci.* 15, 20 (2011).

33. J. Wang, I.J. Beyerlein, N.A. Mara, and D. Bhattacharyya, *Scr. Mater.* 64, 1083 (2011).
34. J. Wang, R.G. Hoagland, and A. Misra, *Appl. Phys. Lett.* 94, 131910 (2009).
35. S. Mahesh, C.N. Tomé, R.J. McCabe, G.C. Kaschner, I.J. Beyerlein, and A. Misra, *Metall. Mater. Trans. A* 35A, 3763 (2004).
36. D.J. Alexander and I.J. Beyerlein, *Mater. Sci. Eng. A* 410, 480 (2005).
37. P.M. Anderson, J.F. Bingert, A. Misra, and J.P. Hirth, *Acta Mater.* 51, 6059 (2003).
38. D. Raabe, F. Heringhaus, U. Hangen, and G. Gottstein, *Z. Metallkd.* 86, 405 (1995).
39. A.F. Voter, Los Alamos Unclassified Technical Report No. LA-UR 93-3901 (1993).
40. G.J. Ackland and R. Thetford, *Philos. Mag. A* 56, 15 (1987).
41. R.F. Zhang, J. Wang, I.J. Beyerlein, and T.C. Germann, *Philos. Mag. Lett.* 91, 731 (2011).
42. F. Cao, I.J. Beyerlein, F.L. Addessio, B.H. Sencer, C.P. Trujillo, E.K. Cerreta, and G.T. Gray III, *Acta Mater.* 58, 549 (2010).
43. I.J. Beyerlein, N.A. Mara, D. Bhattacharyya, C.T. Necker, and D.J. Alexander, *Int. J. Plast.* 27, 121 (2011).
44. N.A. Mara, I.J. Beyerlein, J.S. Carpenter, and J. Wang, *JOM* (2012). doi:[10.1007/s11837-012-0430-1](https://doi.org/10.1007/s11837-012-0430-1).
45. N. Li, N.A. Mara, J. Wang, P. Dickerson, J.Y. Huang, and A. Misra, *Scr. Mater.* 67, 479 (2012).
46. A. Misra, J.P. Hirth, R.G. Hoagland, J.D. Embury, and H. Kung, *Acta Mater.* 52, 2387 (2004).
47. S.C.V. Lim and A.D. Rollett, *Mater. Sci. Eng. A* 520, 189 (2009).